Optimum design and performance of a solar dish microturbine using tailored component characteristics

Giacomo Gavagnin[a], Sergio Rech[b], David Sánchez[a,*], Andrea Lazzaretto[c]

[a] *University of Seville, Camino de los descubrimientos s/n, 41092 Seville, Spain*
[b] *Interdepartmental Center "Giorgio Levi Cases" for Energy Economics and Technology - University of Padova, via Marzolo 9, 35131 Padova, Italy*
[c] *Department of Industrial Engineering - University of Padova, via Venezia 1, 35131,Padova, Italy*

Abstract

The aim of the paper is to find the optimum design and performance of solar microturbines powered by parabolic dish collectors using an innovative methodology which integrates the design and off-design models of the total system. In contrast to the common practice of assigning an estimated efficiency to the engine turbomachinery (generalized performance maps), the procedure hereinafter produces the specific geometry and the characteristic maps of compressor and turbine, according to their inlet/outlet thermodynamic states and working cycle boundary conditions.

With this global approach, a sensitivity analysis is performed to search for the pressure ratio that maximizes the solar-to-electric efficiency at design point for a constant air mass flow rate and turbine inlet temperature. Maximum values in the range 18.0% to 21.7% are obtained for a pressure ratio of 3.2 when the turbine inlet temperature changes between 800°C (*base-case* system) and 900°C.

The methodology allows also to simulate the performance of the system when different design $DNIs$ are considered with the aim to maximize the annual yield of the system. Simulations performed for Beijing, Seville and San Diego showed that quite different $DNIs$ (610 to 815 W/m^2) are to be chosen to get the maximum annual (average) efficiency: 11% to 16% for the base-case system and 14% to 19% for a more advanced design.

*Corresponding author
Email address: ds@us.es (David Sánchez)

Keywords: Microturbine, Solar dish, Volumetric cavity receiver, Design and off-design

NOMENCLATURE

α	Absorptivity
$\bar{\eta}_{global}$	Mean annual efficiency (global)
$\bar{T}_{air}$	Average temperature of air in the cavity of the solar receiver
Δh_s	Isentropic enthalpy change
δ_{cl}	Clearance gap
$\dot{C}$	Heat capacity
$\dot{m}$	Mass flow rate
$\dot{Q}_{int}$	Receiver gross heat input
$\dot{v}$	Volumetric flow rate
ϵ	Emissivity
η	Efficiency
Γ	Flux capture fraction
γ	Heat capacity ratio
$\nu_{ts,t}$	Total-to-static velocity ratio
ω	Angular rotational speed
ϕ	Total radiant flux
ψ	Rim angle
ρ	Density
σ	Stefan-Boltzmann constant
τ	Transmissivity
ε	Effectiveness
ς	Reflectivity
ξ	Inclination angle
A	Aperture area
amb	Ambient
b_{blade}	Blade height
C^*	Heat capacity ratio
$c_{0,is}$	Spouting velocity
d	Diameter
d_s	Specific diameter
DNI	Direct Normal Irradiance
DP	Design Point
E	Energy
e_{tot}	Total concentration error
f_p	Pressure loss factor
$f_{capacity}$	Capacity factor
f_{dish}	Focal distance of dish
f_{dumped}	Dumped energy factor
G	Specific flow rate
h	Enthalpy
HTA_{rec}	Heat Transfer Area of recuperator

I	Specific irradiance
$k_{cv,ext}$	External convective heat transfer coefficient of receiver window
$k_{cv,int}$	Internal convective heat transfer coefficient of receiver window
k_{dep}	Derating factor
mGT	micro Gas Turbine
N	Rotational speed
n_s	Specific speed
NTU	Number of Transfer Units
P	Power
p	Pressure
P_{mech}	Shaft power
r_c	Compressor pressure ratio
r_e	Turbine pressure ratio
rcv	Receiver
rec	Recuperator
rel	Relative
SR	Simple recuperated
T	Temperature
T_w	Temperature of glass window of solar receiver
TIT	Turbine Inlet Temperature
TMY	Typical Meteorolgical Year
TOT	Turbine Outlet Temperature
ts	Total-to-static
tt	Total-to-total
U	Heat transfer coefficient
u	Blade speed
v_{cr}	Critical speed
W	Specific power

1. Introduction

Solar power is the most abundant and distributed primary energy source on Earth. In the last decades, academic and governmental organizations have attempted to develop power systems able to collect and convert this energy into electricity. Many of these efforts were aimed at demonstrating the technical and economic feasibility of systems that integrate solar energy collection and concentration devices with well established power generation systems. Among these conventional technologies, the focus has always been on the utilization of gas turbines for their small footprint and low capital cost [1–5].

One of the most recent attempts to develop small scale solar power generators based on micro gas turbine technology is the OMSoP project (*Optimised Microturbine Solar Power Generator*), funded by the European Commission within the 7^{th} Framework Programme [6]. The OMSoP consortium has already published many works related to this type of systems

[7–12]. Giovannelli [7, 8] presents a review of the current state of the art in the area of small-scale concentrated solar thermal power systems based on dish collectors. Lanchi et al. [9] present the experimental solar unit developed by ENEA (Italian National Agency for New Technologies, Energy and Suitable Economic Development) for the OMSoP project. Cerri et al. [10] propose the integration of solar dishes with advanced semi-closed cycles micro-turbines. Sanchez et al. [11] analyze the potential of selected markets for the worldwide commercial deployment of OMSoP systems. Gavagnin et al. evaluate the manufacturing, transportation and installation costs of the simple recuperated solar-only and hybrid systems in [12] and the economic and financial appraisal of the project for simple recuperated, intercooled and intercooled/reheated advanced layouts in [13].

Micro gas turbines (mGT) have power outputs in the range from a few kilowatts [14] to half a megawatt [15], even if this upper limit might change between 250 kW and 1 MW depending on the source. They typically include single stage radial turbomachinery with moderate pressure ratio (though higher pressure ratios are possible in larger engines in combination with axial flow machinery) and an internal heat recovery device (compact heat exchanger [14]) to enhance efficiency. These components are typically arranged in a single shaft configuration although multiple-shaft layouts have also been considered [16].

Solar micro turbines typically make use of parabolic dish collectors to collect and concentrate solar energy onto a receiver which in turn converts it into heat. The concentration ratio of these collectors is very high and enables the very high temperature that is needed to attain high efficiency [17]. With the aforecited OMSoP project, the Royal Institute of Technology in Stockholm (KTH) tested two different solar receiver prototypes: a cavity volumetric pressurized receiver with foam absorber [18, 19] and an impingement cavity receiver [20]. The integration of volumetric receivers in several applications such as solar systems for off-grid energy production [21] and polygeneration in rural areas [22], either in simple or combined cycle configuration [23], was studied by Aichmayer et al. whilst Wang et al. [24] investigated an integrated dish-mGT design using solar systems with impingement receivers. These activities add to the past work on these systems for space, military and civil power applications: Kesseli et al. calculated the performance of a micro turbine engine composed by stock turbocharger components in [25] while Dickey presented the experimental performance of a Capstone micro turbine integrated with a field of heliostats in [26]. More recently, LeRoux and Meyer

made use of a lumped-volume approach to simulate the performance of a small-scale dish-mTG system using data from standard off-the-shelf Garrett turbocharger technology and a model of open-cavity tubular receivers [27]. Semprini et al. also employed models of solar-only and hybrid mGT systems based on lumped volumes and turbomachinery performance maps taken from literature [28].

In contrast to these past works, which rely on generalized performance maps of turbomachinery or on existing compressors/turbines (engines derived from turbochargers), the current paper presents a two-step integrated procedure i) to design solar mGT systems by determining optimum turbomachinery geometries and performance maps, and ii) to simulate the off-design behavior in order to evaluate the highest annual production of electricity for a specific location.

This integrated approach to the design and off-design analyses of solar mGTs allows for the generation of "ad hoc" designs for a specific location and for the calculation of more reliable performance values along a typical year of operation as compared to those calculated with the "traditional" approach.

2. Dish-mGT integrated solar systems

Power generators based on integrated dish-mGT systems are mostly based on the simple recuperated Joule-Brayton cycle, Fig. 1, even if other configurations including intercooling and reheat have been proposed in the literature [10, 13, 29].

The parabolic dish is responsible for the heat supply and is a well established technology with many different designs having been tested in the past. Most of this experimental activity aimed at the integration in dish-Stirling systems [30–32] but there are also prototypes with micro turbines. A complete dish-mGT assembly based on an engine derived from a turbocharger was studied in the mid 1980s by NASA (National Aeronautics and Space Administration) in the *Brayton Power System* and *Solar Advanced Gas Turbine Engine* projects [33, 34]. Amsbeck et al. reported the testing of a solar-hybrid mGT at the Plataforma Solar de Almeria [35] and Dickey et al. published test results of an adapted Capstone mGT operated on solar energy at the Weizmann Institute [36]. Finally, Kesseli et al. reported tests carried out by Brayton Energy with a system including dish collectors, micro gas turbines and a compressed air storage system [37]. Most of these units make use of solar volumetric receivers because of the higher efficiency as compared

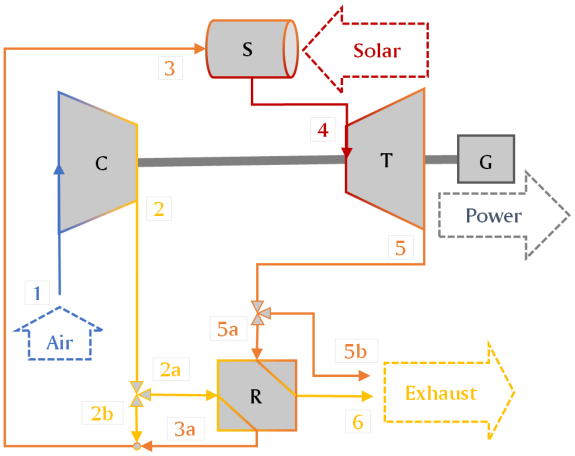

Figure 1: Single-shaft recuperative microturbine with integrated solar receiver: compressor (C), recuperator (R), solar receiver (S), turbine (T) and generator (G).

to cavity receivers in either tubular or impingement configuration [38, 39]. The knowledge gained from these experimental activities is complemented by the thorough theoretical analysis exploring the advantages and disadvantages of using adapted turbochargers or small gas turbines designed from scratch [40–45].

In the recuperated Brayton-Joule cycle shown in Fig. 1, the available heat carried by the gases leaving the expander is used to preheat the air delivered by the compressor before this enters the combustor, with the aim to increase the thermal efficiency of the engine. This layout is best exploited when associated with low pressure ratios which enable the utilization of single-stage radial turbomachinery coupled to a solar receiver as a mere substitute for the combustor of a conventional mGT [16]. The flow diagram is as follows. Ambient air enters the compressor (C) where it is pressurized (1-2). This air stream then flows into the cold side of the counter-flow compact recuperator (R) where it is heated by the hot exhaust air flowing out from the turbine (2a-3a). Once preheated, the air enters the solar receiver (S) where it is heated up further by the solar energy collected by the parabolic dish and concentrated onto the focal point where the solar receiver is mounted. This component is a volumetric, pressurized receiver with a SiC foam absorber and a quartz glass window that lets solar energy in whilst reducing both pressure and convective heat losses. The concentrated solar beams entering the receiver heat the foam absorber which, in turn, raises the temperature

of air flowing through it (air acts as a coolant for the absorber). The air exiting the receiver flows into the turbine (T) where it is expanded (4-5) and then sent to the hot end of the recuperator where it is cooled down by the compressor delivery air before being released to the atmosphere (5a-6). When the available solar radiation exceeds a maximum value (upper threshold), a fraction of the total mass flow through the engine bypasses both sides of the recuperator, thus reducing the inlet temperature to the solar receiver (3) and avoiding overheating of the system. The electric generator (G) is mounted on the same shaft as the turbine and compressor, hence rotating at a very high, variable speed (in the range 100-150 krpm). This means that power electronics are required to ensure that voltage and frequency of the electric output are stable and in compliance with the requirements of the grid.

Two technology levels of the mGT are considered here, corresponding to different values of turbine inlet temperature (TIT) and recuperator effectiveness ($\varepsilon_{rec,DP}$): *base-case* (800°C-85%) and *advanced* system (900°C-90%). This choice is based on techno-economic considerations. Temperatures lower than 800°C would bring about a drastic efficiency drop whereas temperatures above 900°C would imply using more expensive ceramic materials in the turbine [16, 46]. Recuperator effectiveness lower than 85% would bring a too low internal heat recuperation whereas a value higher than 90% would imply a very heavy and expensive component [16, 47].

Figure 2 shows the thermodynamic cycles of both the *base-case* and *advanced* systems. The differences lay on the position of station 4 (TIT effect) and in the relative position of station 5 with respect to station 3 (effect of $\varepsilon_{rec,DP}$). The main deign specifications of the system are summarized in Table 1, where the range of DNI (DNI_{DP}) and pressure ratio ($r_{c,DP}$) considered in the sensitivity analysis are also given.

Main system specifications			
DNI_{DP}	800 W/m^2	(sensitivity 400 W/m^2-1000 W/m^2)	
$r_{c,DP}$	3	(sensitivity 2.5-4)	
$\dot{m}_{air,DP}$	0.1 kg/s		
TIT_{DP}	800 °C (*base*) 900 °C (*adv.*)	$\varepsilon_{rec,DP}$	85 % (*base*) 90 % (*adv.*)
$T_{amb,DP}$	25 °C	$p_{amb,DP}$	101325 Pa
$f_{p,rec,c,DP}$	97.0 %	$f_{p,rec,h,DP}$	98.5 %
$f_{p,rcv,DP}$	96.0 %	$f_{p,in/out,DP}$	99.5 %
$\eta_{mech,DP}$	99.0 %	$\eta_{el,DP}$	90.0 %
$\Delta T_{turb,DP}$	5 °C	$n_{s,t,DP}$	0.55

Table 1: Independent variable set (input parameters).

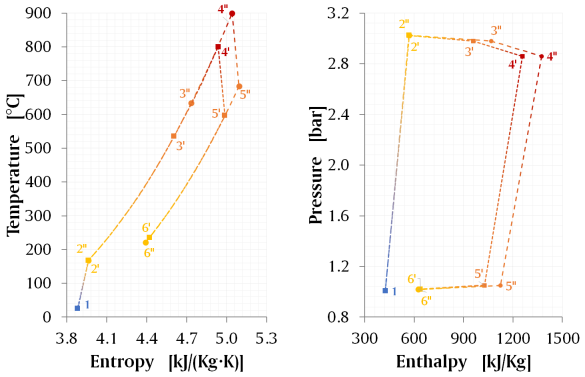

Figure 2: Temperature-entropy (left) and pressure-enthalpy (right) diagrams of the *base-case* and *advanced* systems.

3. Methodology

The methodology used to find the optimum design and performance of the solar-mGT system is based on an integrated procedure which combines the design and off-design performances of the system. Both models are solved with a modular-sequential approach which relies on the conservation of mass, momentum and energy and on established correlations to characterize components performance and efficiency. The working fluid is air which is considered to be dry real gas with the thermodynamic properties provided by Coolprop® [48]. The complete model is implemented in Matlab® on the assumption that all processes take place in equilibrium [49].

The first stage of the design model consists in calculating the working cycle and the characteristics of the main system components. To this end, both one dimensional (1-D) and zero dimensional (0-D) approaches are used: radial turbomachinery (1-D), solar receiver (0-D), recuperator (0-D) and solar dish (0-D). The design space is limited by a sufficiently large range of pressure ratios (2.5-4, see Section 5.1) wherein potential designs are explored in order to attain the highest solar-to-electric efficiency at the design point. The basic geometry of the turbomachines, which includes the meridional flow path and blades, is then used to produce the corresponding performance maps that will later be used by the off-design model (see Fig. 4) to evaluate the behavior of the system when subjected to boundary conditions different from the design ones. This off-design model relies on a suitable control strategy which ensures the safe operation of the system within a certain range of

boundary conditions.

3.1. Design model

The structure of the design model shown in the flowchart in Fig. 3 is common to the *base-case* and *advanced* systems (Section 2) and the input data to the model are listed in Table 1. Upon calculation of the working cycle with the input data in Table 1, the *"Thermodynamic cycle 1"* module calculates the inlet conditions (pressure and temperature) to each turbomachinery along with the corresponding turbine expansion ratio ($r_{e,DP} = p_4/p_5$) for a given pressure ratio of the compressor ($r_{c,DP} = p_2/p_1$). Pressure losses across the solar receiver, recuperator and inlet/outlet ducts are taken into account by means of the pressure loss factors ($f_p = p_{out}/p_{in}$) in Table 1. With this information, the turbomachinery 1-D design modules (*"Turbine"* and *"Compressor"*) calculate the draft geometries of turbine and compressor, also providing their isentropic efficiencies and rotational speed. These data are then used to complete the simulation of the thermodynamic cycle by calculating the outlet states of each turbomachinery and the complete heat balance of the recuperator. With the thermodynamic cycle calculated fully, the recuperator is designed using the $\varepsilon - NTU$ approach to calculate the Number of Transfer Units (NTU). This provides the total heat transfer area of the selected counter-flow configuration that yields the target effectiveness specified originally.

The tools to design the solar subsystem include the parabolic dish and receiver modules. The aperture (dish) and window (receiver) area of these elements are optimized for the nominal conditions obtained in the design model of the mGT by minimizing of heat losses. Inputs to the parabolic dish model are the design DNI and the heat input to the receiver with which the receiver model calculates the air outlet temperature (TIT). Two iterative loops are finally used to optimize the aperture area of collector and receiver:

1. The inner loop searches for the optimum size of the receiver. This stems from a balance between heat input from the collector and heat losses to the environment.
2. The outer loop corrects the dish aperture area until the receiver outlet temperature is equal to the specified TIT at the rated conditions.

A detailed description and the equations of the design models of the mGT components are given in Appendix A.

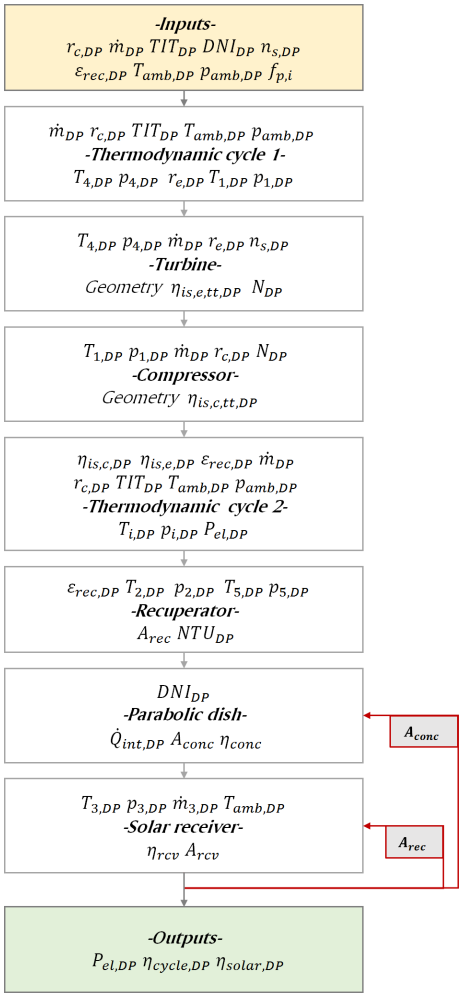

Figure 3: Flowchart of the design model.

3.2. Off-design model and control strategy

The off-design model of the solar-mGT system is built according to the iterative procedure shown in Fig. 4. Input data are the external conditions (DNI, T_{amb}) in addition to the thermodynamic states of the cycle, the geometric characteristics and performance maps of compressor and turbine calculated in the design procedure (Section 3.1), and the performance maps of the electric generator, solar receiver and recuperator derived from experimental information. All the off-design submodels of the components are presented in Appendix B.

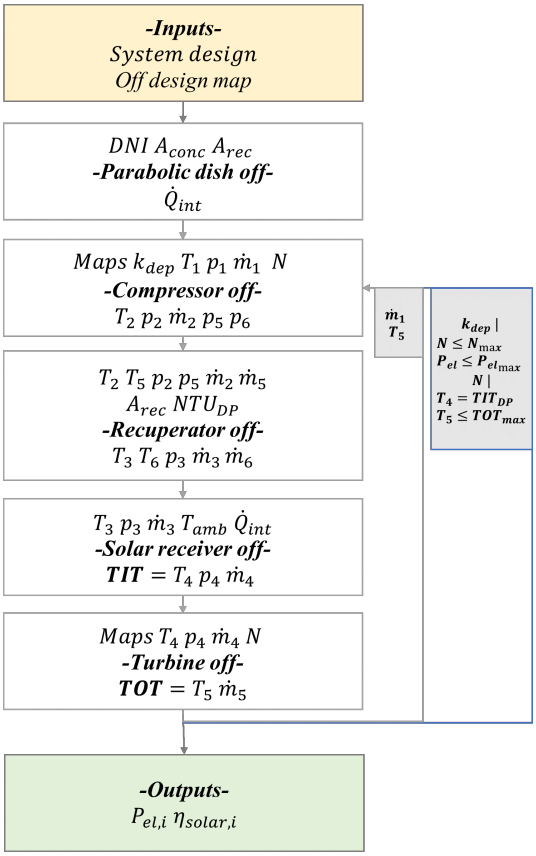

Figure 4: Flow chart of the off-design model.

The calculations of the model are complemented by appropriate numerical and control strategies made up of two iterative loops. The inner loop, shown grey in Fig. 4, exchanges information between the recuperator and expander

and is used to calculate the turbine outlet temperature ($TOT = T_5$) and the air mass flow rate at equilibrium ($\dot{m}_1$). TOT is a required input to solve the regenerator submodel but it also depends on the off-design performance of the expander downstream. At the same time, $\dot{m}_1$ depends on the pressure ratio and shaft speed of compressor and turbine, bringing in a cross-dependence between the operating points of both components. The inner loop starts with guessed values of both variables (TOT,$\dot{m}_1$) and iterates through corrections until convergence is reached.

The outer iterative loop, blue line in Fig. 4, is used to implement the control strategy that maximizes the efficiency of the system and avoids non-feasible or hazardous operating conditions. This strategy is based on keeping turbine inlet temperature ($TIT = T_4$) at the rated value through variations of shaft speed (N) which, as expected, bring about similar changes in both the enthalpy change and throughput across the compressor and expander. This is valid for any set of boundary conditions as long as specific (upper) thresholds of the following critical variables are not exceeded: turbine outlet temperature (TOT), electric output (P_{el}) and shaft speed (N).

Indeed, a maximum TOT (TOT_{max}) is introduced to prevent overheating of the recuperator since this temperature is actually the inlet temperature to the hot end of the heat exchanger: TOT_{max}=675°C for the *base-case* (347 stainless steel) and TOT_{max}=750°C for the *advanced* system (super 347 stainless steel) according to McDonald [50]. In practice, this limit can potentially be exceeded at $DNI < DNI_{DP}$, when the air flow rate through the solar receiver ($\dot{m}_3 = \dot{m}_1$) and shaft speed (N) are reduced in order to keep TIT at the rated value. This results in a reduction of the engine pressure ratio following the performance maps of compressor and expander (see Fig. 5) and, in turn, TOT increases. Eventually, when the upper limit is reached, the control strategy of shaft speed changes so as to keep TOT at the maximum value (Figs. 6 and 7).

Upper limits of shaft power P_{mech} and N are also in place to prevent overloading of the electric generator and overspeeding of the rotating components for $DNI > DNI_{DP}$. N_{max} is set to 115% the rated value while $P_{mech,max}$ is calculated as a function of N (see Appendix B.2). When $P_{mech,max}$ and/or N_{max} are reached, the recuperator is bypassed to a certain fraction (a similar fraction of the hot and cold flows are diverted to their corresponding outlets) as discussed in Section 2. This results in a reduction of the air temperature at the inlet (and most likely the outlet) of the solar receiver which implies a reduction in both N and P_{el}. A control parameter k_{dep} is

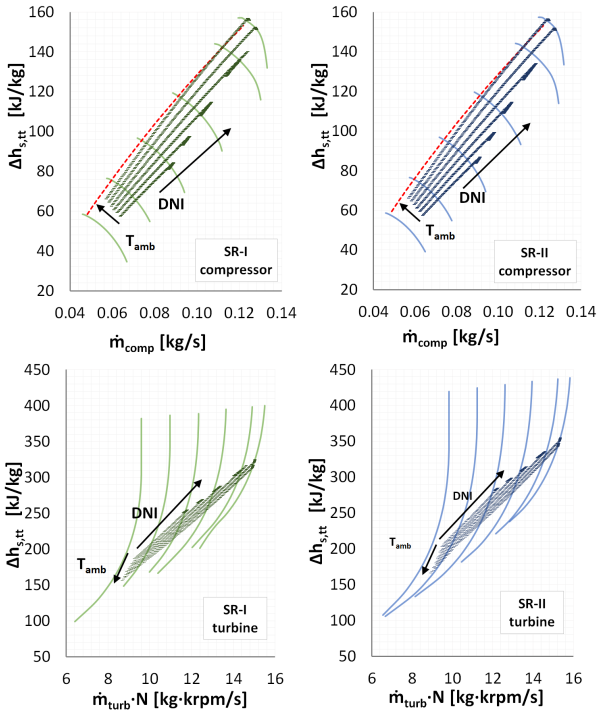

Figure 5: Corrected performance maps used for the off-design model of compressor (above) and turbine (below) for the *base-case* (left) and *advanced* (right) systems.

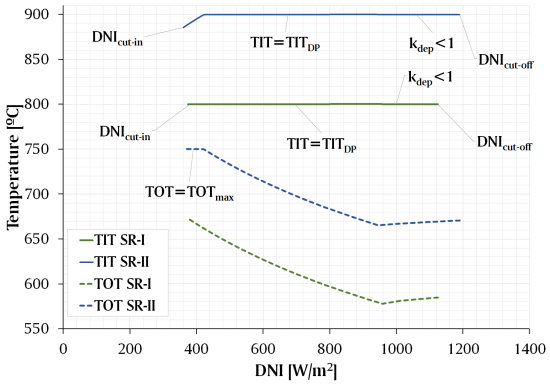

Figure 6: Off-design turbine inlet (TIT) and outlet (TOT) temperatures vs. DNI at rated ambient temperature ($T_{amb,DP}$) for the *base-case* (green) and *advanced* (blue) systems.

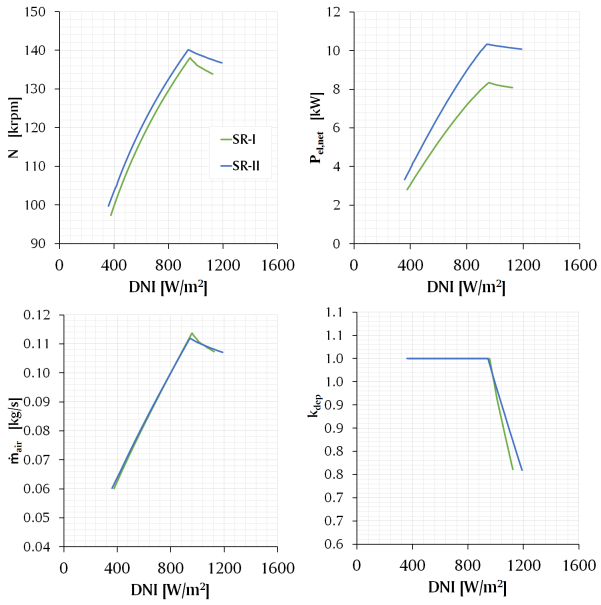

Figure 7: Main control variables (values relative to design point) of the system vs. DNI at $T_{amb,DP}$.

introduced in the outer loop to evaluate the amount of air mass flow rate that is bypassed at the recuperator. It is defined as the ratio of mass flow rate that enters the recuperator to total mass flow rate at compressor outlet ($k_{dep} = \dot{m}_{2a}/\dot{m}_2$). It is also assumed that the system is shut down for $k_{dep} < 0.75$ or for $N/N_{DP} < 0.75$. A comparative study of the control strategies for pure solar microturbine systems, including recuperator by-pass, has recently been published by Ghavami et al. [51].

Figures 6 to 8 show the performance of the system when the aforedescribed control strategy is implemented, both for the *base-case* and *advanced* systems. The plots consider variable DNI and constant ambient temperature (25°C). It is worth noting that the limit TOT is reached only in the *advanced* system and for DNI<420 W/m^2.

4. Validation of numerical models

The numerical models of the complete dish-mGT system cannot be validated directly because there are no systems of the same size available in the market nor are theoretical data available in literature. Nevertheless, the

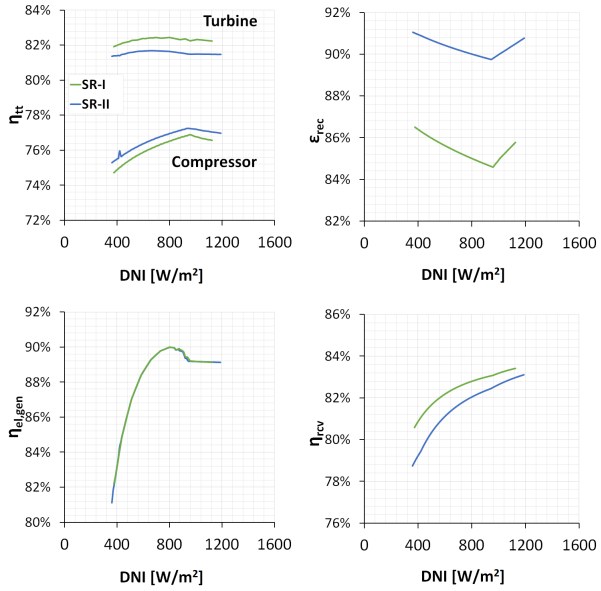

Figure 8: Main component efficiencies of the system vs. DNI at $T_{amb,DP}$. Clockwise from top left: total to total efficiency of turbomacinery, recuperator effectiveness, electric efficiency of generator, thermal efficiency of solar receiver.

individual models of the constituents were previously validated against theoretical or experimental data and hence the model of the complete system is expected to provide trustful results. In particular:

- The performance models of the compressor and turbine are well known and have been validated by Aungier against a large set of experimental data taken from real applications [52, 53]. Moreover, the specific models of the compressor developed for the solar application have been validated in a previous work for air and sCO_2 [54]. For the turbine, a specific validation against experimental data was done by NASA, as a function of the relative size of the clearance gap. The total-to-total and total-to-static efficiencies at the design point obtained experimentally [55], the results of the model and the corresponding errors are shown in Table 2.

$\delta_{cl,rel}$	Ref [55]	Model	Error
Total-to-total efficiency			
0.25%	89.2%	90.2%	1.05%
3%	84.7%	86.0%	1.62%
7%	79.3%	82.3%	3.64%
Total-to-static efficiency			
0.25%	87.0%	84.1%	3.51%
3%	82.8%	80.5%	2.88%
7%	77.7%	77.0%	0.87%

Table 2: Validation of turbomachinery design models.

- The design and off-design models of the solar components (parabolic dish and volumetric receiver) have both been validated against data obtained at the test rig at the Royal Institute of Technology in Stockholm (KTH) [18, 19].

- The off-design model of the electric generator is derived from experimental data obtained by ENEA directly [8].

- The properties of dry air with real gas behavior are computed with Coolprop® whose accuracy is widely acknowledged within the industrial and scientific communities [48].

5. Results

This last Section presents three different sets of results:

1. The results obtained by running the design model for the *base-case* ($TIT = 800°C$ and $\varepsilon_{reg,DP} = 0.85$) and *advanced* ($TIT = 900°C$ and $\varepsilon_{reg,DP} = 0.90$) systems for a design DNI of 800 W/m^2 and an air flow rate of 0.1 kg/s (see Table 1). In this analysis, the sensitivity to the rated pressure ratio is also assessed.
2. The off-design performance maps and the results of the annual simulation of the two systems mentioned in the previous bullet point.
3. The results of a sensitivity analysis with respect to the design DNI for three different locations (Beijing, Seville and San Diego).

5.1. Results at the design point

The following performance metrics are used to characterize the aforecited systems:

- The global (solar-to-electric) efficiency (η_{global}) is defined as the ratio from net electric output (P_{el}) to total heat input to the system ($DNI \cdot A_{dish}$), Eq. (1). It can be applied to either design or off-design conditions.

- The specific output can be referred to the air mass flow rate ($\hat{P}_{el}$, Eq. (2)) or to the aperture area of the parabolic dish ($\hat{P}_{solar,DP}$, Eq. (3)). It can also be applied to either design or off-design conditions.

- The efficiencies of the parabolic dish collector ($\eta_{dish,DP}$), solar receiver ($\eta_{rcv,DP}$) and mGT ($\eta_{mGT,DP}$), defined by Eqs. (4-6).

$$\eta_{global} = \frac{P_{el}}{DNI \cdot A_{dish}} \tag{1}$$

$$\hat{P}_{el} = \frac{P_{el}}{\dot{m}_1} \tag{2}$$

$$\hat{P}_{solar} = \frac{P_{el}}{A_{dish}} \tag{3}$$

$$\eta_{dish} = \frac{\dot{Q}_{int,DP}}{DNI_{DP} \cdot A_{a,dish}} \tag{4}$$

$$\eta_{rcv,DP} = \frac{\dot{Q}_{mgt,DP}}{\dot{Q}_{int,DP}} \tag{5}$$

$$\eta_{mGT,DP} = \frac{P_{el,DP}}{\dot{Q}_{mgt,DP}} \tag{6}$$

A complete sensitivity analysis of system and component performance against pressure ratio ($r_{c,DP}$) is shown in Fig. 9 for the *base-case* and *advanced* systems (green and blue lines respectively). Firstly, it is worth noting that both systems achieve maximum η_{global} for a pressure ratio of about 3.2, even if a higher pressure ratio would have been expected for the *advanced* case. This is mostly because of the higher recuperator effectiveness of the *advanced* case which promotes a lower pressure ratio to exploit the recuperative potential fully, Table 1. The efficiency of the parabolic dish is independent from $r_{c,DP}$ as shown in Section Appendix A.5, whereas the efficiency of the receiver increases slightly with pressure ratio because of the higher density of air. Shaft speed also increases because more compression work is needed whereas the aperture areas of dish and receiver increase with $r_{c,DP}$ due to the higher heat input that comes about because of the decreasing inlet temperature to the receiver (lower turbine exhaust temperature).

In the light of the information in Fig. 9 and in order to maintain a feasible shaft speed of some 130 krpm, a lower pressure ratio equal to 3 is finally selected, even if the rated efficiency shown is slightly lower than the optimum value.

Table 3 summarizes the dependent variables calculated in the design process. The *base-case* system produces more than 7 kW_e with an aperture area of 50 m^2 while the *advanced* system generates almost 9 kW_e (about 25% more) with a 3% larger aperture area only. This power gain is mainly due to the higher TIT and $\epsilon_{reg,DP}$ which raise the mean temperature of heat addition to the working cycle, transformations $3' - 4'$ and $3'' - 4''$ in Fig. 2.

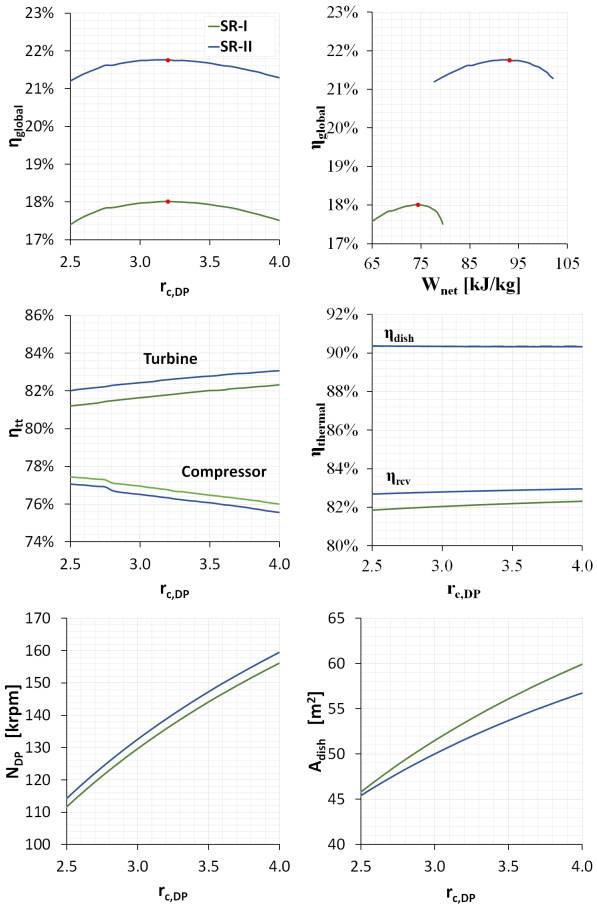

Figure 9: Global (solar-to-electric) efficiency vs. pressure ratio and specific power (above), turbomachinery total-to-total efficiencies vs. pressure ratio (center) and shaft speed and dish/receiver aperture areas vs. pressure ratio (below). *Base-case* and *advanced* systems shown in green and blue respectively.

Base-case system			
$P_{el,DP}$	7.19 kW_e	$\eta_{s,t,DP}$	82.44 %
A_{dish} (d_{dish})	50.0 m^2 (8.0 m)	$\eta_{s,c,DP}$	76.52 %
A_{rcv} (d_{rcv})	167 cm^2 (14.6 cm)	$\eta_{dish,DP}$	90.35 %
HTA_{rec}	5570 m^2	$\eta_{rec,DP}$	82.79 %
$NTU_{rec,DP}$	5.45	$\eta_{mGT,DP}$	24.03 %
N_{DP}	129690 rpm	$\eta_{global,DP}$	17.97 %
$\hat{P}_{sol,DP}$	0.144 kW_e/m^2	$\hat{P}_{el,DP}$	71.9 $kW_e/(kg\cdot s)$
Advanced system			
$P_{el,DP}$	8.96 kW_e	$\eta_{s,t,DP}$	81.64 %
A_{dish} (d_{dish})	51.5 m^2 (8.1 m)	$\eta_{s,c,DP}$	76.97 %
A_{rcv} (d_{rcv})	171 cm^2 (14.8 cm)	$\eta_{dish,DP}$	90.34 %
HTA_{rec}	8757 m^2	$\eta_{rec,DP}$	82.04 %
$NTU_{rec,DP}$	8.58	$\eta_{mGT,DP}$	29.34 %
N_{DP}	132540 rpm	$\eta_{global,DP}$	21.74 %
$\hat{P}_{sol,DP}$	0.174 kW_e/m^2	$\hat{P}_{el,DP}$	89.6 $kW_e/(kg\cdot s)$

Table 3: Main design specifications of the *base-case* and *advanced* systems for 800 W/m^2 and the optimum $r_{c,DP}$.

5.2. Results of the annual simulations

The off-design model shown in Section 3.2 is used here to calculate the solar-mGT performance maps linking power output and efficiency to the DNI at given ambient temperatures. These maps are then utilized to evaluate the annual yield (production of energy) for given annual distributions of DNI and ambient temperature in a specified location.

In order to analyze the results of the off-design model, the following three additional performance metrics are introduced:

- The mean annual conversion efficiency ($\bar{\eta}_{global}$, Eq. (7)) is the ratio from the net annual electricity ($E_{el,net}$) to the available solar energy input (E_{sol}) over the year. It must be noted that the latter may differ from the solar energy actually harvested by the system (Q_{sol}) due to periods when the system is not in operation because of the very high or very low DNI: $DNI < DNI_{cut-in}$ or $DNI > DNI_{cut-off}$, Fig. 6.

- The capacity factor of the system ($f_{capacity}$, Eq. (8)) is the ratio from the annual yield ($E_{el,net}$) to the electric energy that would be produced if the system worked at the nominal output ($P_{el,DP}$) throughout the year (8760 hours).

- The dumped solar energy factor f_{dumped}, Eq. (9), is the ratio from the solar energy that is available but not harvested by the system ($E_{sol} - Q_{sol}$) to the available solar energy input (E_{sol}). This metric is used to

quantify the fraction of available solar energy that cannot be harvested because the system is already running at full or minimum capacity.

$$\bar{\eta}_{global} = \frac{E_{el,net}}{Q_{sol}} \tag{7}$$

$$f_{capacity} = \frac{E_{el,net}}{P_{el,DP} \cdot 8760} \tag{8}$$

$$f_{dumped} = 1 - \frac{E_{sol} - Q_{sol}}{E_{sol}} \tag{9}$$

Figure 10 shows the performance maps obtained for the *base-case* (green) and *advanced* (blue) systems. The inability to absorb a very high radiation becomes evident in the upper charts and translates into a drastic drop in efficiency (bottom charts) due to a large fraction of the available solar energy that is dumped off by the system at high DNI.

Annual simulations are performed for three selected locations -Beijing (China), Seville (Spain) and San Diego (USA)- for which hourly values of DNI and ambient temperature are obtained from the System Advisory Model software [56]. This information is shown in Fig. 11, whose left chart shows the number of Sun hours (horizontal axis), peak DNI (vertical axis) and annual solar energy available (area subtended by the curve). Similar information is shown for ambient temperature on the right hand side of Fig. 11.

According to the results shown in Table 4, the highest yield is obtained in San Diego where the *base-case* system achieves 15.87% annual conversion efficiency and 24.77% capacity factor, with just 10.69% of the available solar energy being dumped off the system. Seville shows similar performance but, in contrast, the efficiency in Beijing is just 11.13% and the capacity factor is 10.51%, mainly due to the high amount of dumped solar energy (more than 37%). It must be noted that the high f_{dumped} in this location is not due to frequent overflows of solar energy ($DNI > DNI_{cut-off}$) but to long periods of time with DNI lower than the cut-in value ($DNI < DNI_{cut-in}$). Finally, when the *advanced* systems are considered, these yield similar performances in terms of dumped solar energy and capacity factors whereas the annual efficiency is around 2.7-3.5 percentage points higher in all locations.

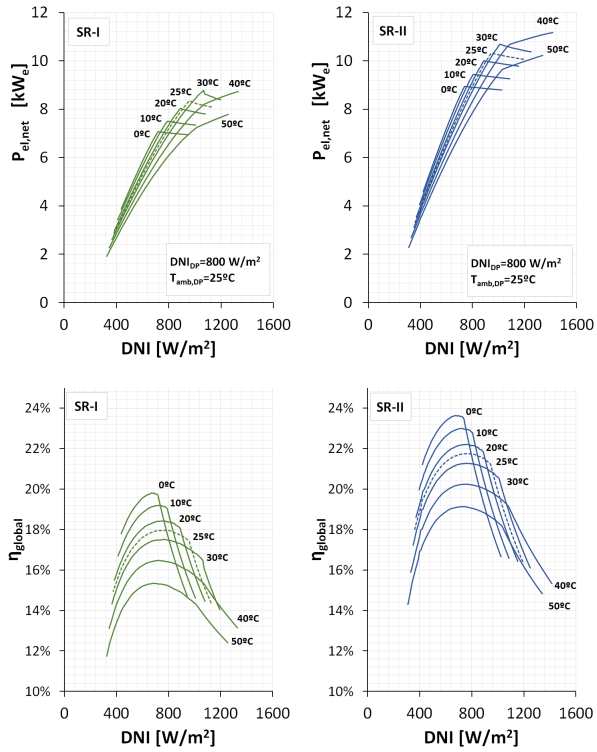

Figure 10: Performance maps of the *base-case* (left) and *advanced* (right) systems: net power output vs. DNI (above) and global (solar-to-electric) efficiency vs. DNI (below)

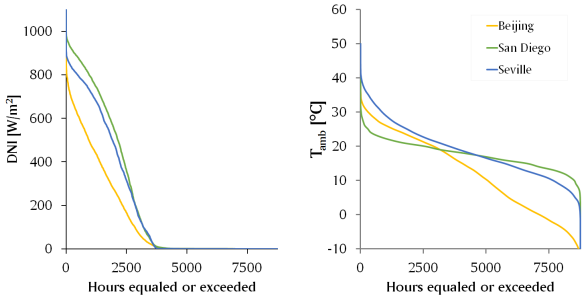

Figure 11: Duration curves of hourly DNI (left) and ambient temperature (right) of the three selected locations in a Typical Meteorological Year (provided by SAM [56]).

Base-case system			
Locations	Beijing	Seville	San Diego
DNI_{DP}[W/m^2]	800	800	800
E_{sol} [kWh]	59494	88676	98304
Q_{sol} [kWh]	37223	76273	87797
$E_{el,net}$ [kWh]	6622	13384	15605
$\bar{\eta}_{global}$	11.13%	15.09%	15.87%
f_{dumped}	37.43%	13.99%	10.69%
$f_{capacity}$	10.51%	21.24%	24.77%
Advanced system			
Locations	Beijing	Seville	San Diego
DNI_{DP} [W/m^2]	800	800	800
E_{sol} [kWh]	61257	91304	101217
Q_{sol} [kWh]	39424	79669	91087
$E_{el,net}$ [kWh]	8463	16938	19581
$\bar{\eta}_{global}$	13.82%	18.55%	19.35%
f_{dumped}	35.64%	12.74%	10.01%
$f_{capacity}$	10.78%	21.58%	24.95%

Table 4: Performance of the *base-case* and *advanced* systems designed for 800 W/m^2 in a Typical Meteorological Year (TMY).

5.3. Sensitivity analysis. Impact of design DNI

Sections 5.1 and 5.2 have shown that largely different performances can be obtained when the same system is operated under dissimilar boundary conditions. For this reason, a sensitivity analysis is now performed in order to assess to what extent the location impacts the reference value of DNI that is convenient to consider in the design process; i.e., DNI_{DP} that yields highest annual efficiency $\bar{\eta}_{global}$, Eq. (7). This metric depends on the hourly distribution of DNI and on the performance maps of the system.

The sensitivity analysis is performed following the procedure shown in Fig. 12. Mass flow rate and turbine inlet temperature are set to their rated values (0.1 kg/s and 800/900 °C for the *base-case*/*advanced* systems respectively) and the value of DNI at the design point (external loop) is changed in the range of interest (400-1000 W/m^2). This means that the micro turbine design remains unaltered with respect to the original design for DNI_{DP}=800 W/m^2 whereas the solar subsystem (parabolic dish and volumetric receiver) is re-sized according to the new value of DNI_{DP}.

The calculations for each DNI_{DP} are based on non-dimensional performance maps of the system, obtained from those shown in Section 3.2 for the reference case at 800 W/m^2. These maps shown in Fig. 10 are then dimensionalized again by merely multiplying the horizontal scale by the corresponding value of DNI_{DP}. Even if the procedure is not utterly accurate,

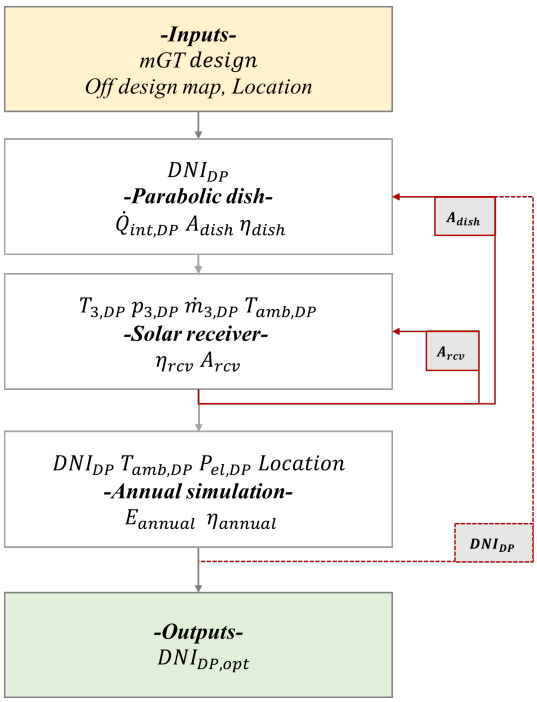

Figure 12: Procedure to search for the optimum DNI_{DP}.

the error incurred does not bring about significant deviations in terms of annual system performance inasmuch as the efficiency of the parabolic dish is rather independent from its size within reasonable limits (see Eqs. (A.15) to (A.16)), while the efficiency of the receiver is only slightly affected by DNI for given TIT and T_{amb}. For the sake of verification of this statement, the performance maps obtained with the non-dimensional approach and those built using the complete off-design procedure in Section 3.2 are shown in solid blue and dotted white lines in Fig. 13, confirming that there is very good agreement in all cases.

The non-dimensional performance maps of the *base-case* and *advanced* systems are shown in Fig. 14 where the non-dimensional power output is plotted against relative DNI for various ambient temperatures. The resulting variations of $\bar{\eta}_{global}$, $f_{capacity}$ and f_{dumped} of the *base case* and *advanced* systems when these performance maps are used are illustrated in Fig. 15. The lower optimal DNI_{DP} is found for Beijing (660 W/m^2 for the *base-case* system and 610 W/m^2 for the *advanced* system) whilst the highest $DNI_{DP,opt}$ corresponds to San Diego (815 W/m^2 for both systems), with Seville laying

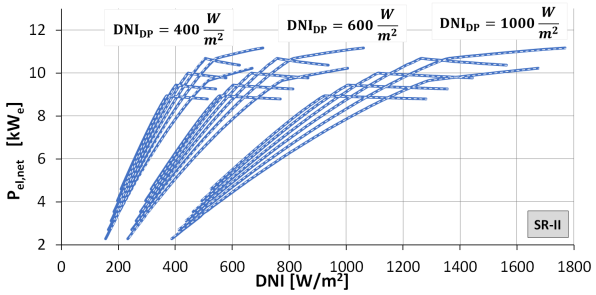

Figure 13: Validation of the performance maps used in the search for the optimum DNI_{DP}: maps calculated with the complete off-design procedure (white dots) and non-dimensional maps (blue line).

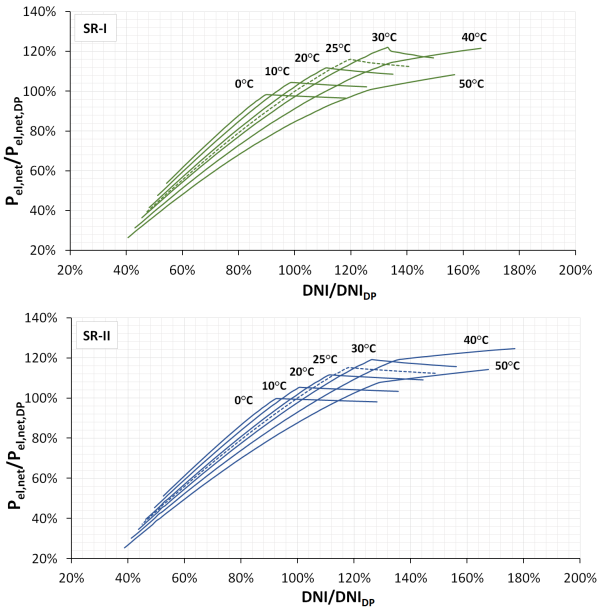

Figure 14: Non-dimensional output of the *base-case* (top) and *advanced* (bottom) systems vs. relative DNI for different ambient temperatures.

in between (715 W/m^2 and 705 W/m^2). The following features of the plots in Fig. 15 are worth noting:

- There exists a visible optimum value of DNI_{DP} for each location. Designing the system for a value different to this one, for instance if a universal DNI_{DP} were used, would inevitably bring about a drastic performance drop ($\bar{\eta}_{global}$).
- The previous statement is stronger in locations with low DNI whereas small changes in DNI_{DP} around the optimum value do not imply a large decrease in $\bar{\eta}_{global}$ if the available DNI is high.
- Interestingly, the values of DNI_{DP} that optimize the capacity factor or dumped solar energy factor in a specific location are generally lower than the value $DNI_{DP,opt}$ that yields highest annual conversion efficiency.

The rated specifications of the dish-mGT systems designed for the optimum DNI_{DP} are summarized in Table 5 while Table 6 shows the corresponding annual performances. It is easily observed that the required dish and receiver aperture areas are larger than those calculated for 800 W/m^2 which brings about a slightly lower nominal solar-to-electric efficiency due to the higher thermal losses (proportional to the receiver area). Nevertheless, in spite of this, there is a significant gain in the annual yield in Beijing and Seville with respect to the reference case with DNI_{DP}=800 W/m^2 (34-48% and 14-16% respectively) while the production of electricity in San Diego remains almost constant. The latter insensitivity is due to the optimum DNI_{DP} in San Diego being close to the reference value of 800 W/m^2. These results underline the importance of a proper selection of DNI_{DP} for each location and turn this parameter into a project-specific design variable.

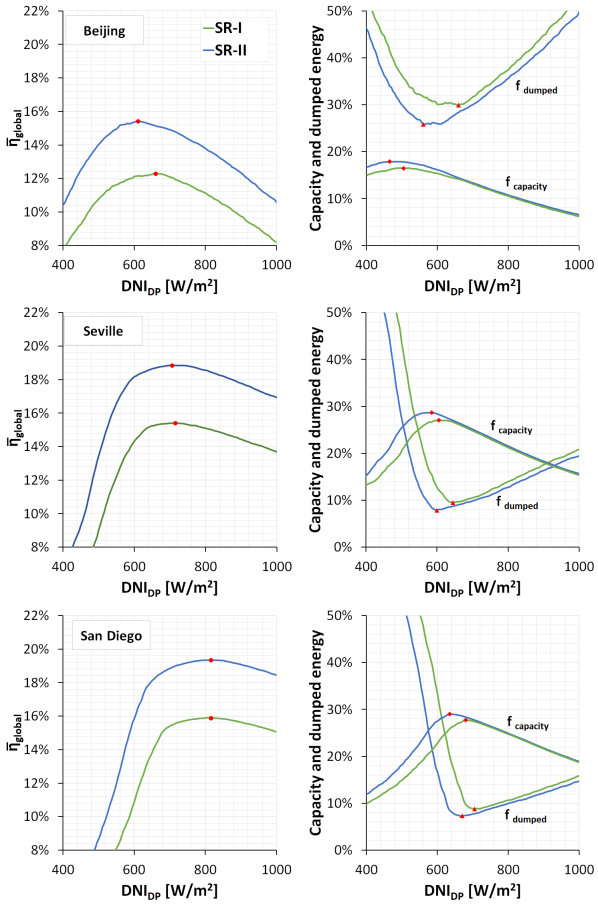

Figure 15: Mean annual global (solar-to-electric) conversion efficiency vs. DNI_{DP} for the three selected locations: *base-case* (blue) and *advanced* (green) systems.

	Base-case system		
	Beijing	Seville	San Diego
DNI_{DP}	660	715	815
A_{dish}	60.9 m^2	56.1 m^2	49.1 m^2
d_{dish}	8.8 m	8.5 m	7.9 m
A_{rcv}	203 cm^2	187 cm^2	164 cm^2
d_{rcv}	16.1 cm	15.4 cm	14.4 cm
$\eta_{dish,DP}$	90.34%	90.34%	90.35%
$\eta_{rcv,DP}$	82.48%	82.62%	82.82%
$\eta_{global,DP}$	17.90%	17.93%	17.98%
	Advanced system		
	Beijing	Seville	San Diego
DNI_{DP}	610	705	815
A_{dish}	68.1 m^2	58.7 m^2	50.5 m^2
d_{dish}	9.3 m	8.6 m	8.0 m
A_{rcv}	227 cm^2	195 cm^2	168 cm^2
d_{rcv}	17.0 cm	15.8 cm	14.6 cm
$\eta_{dish,DP}$	90.33%	90.33%	90.34%
$\eta_{rec,DP}$	81.33%	81.73%	82.08%
$\eta_{global,DP}$	21.55%	21.66%	21.76%

Table 5: Main design specifications of the *base-case* and *advanced* systems at the optimum DNI_{DP}.

	Base-case system		
Locations	Beijing	Seville	San Diego
DNI_{DP} [W/m^2]	660	715	815
E_{sol} [kWh]	72396	99435	96463
Q_{sol} [kWh]	50719	88640	85939
$E_{el,net}$ [kWh]	8895	15320	15334
$\bar{\eta}_{global}$	12.29%	15.41%	15.90%
f_{dumped}	29.94%	10.86%	10.91%
$f_{capacity}$	14.12%	24.32%	24.34%
	Advanced system		
Locations	Beijing	Seville	San Diego
DNI_{DP} [W/m^2]	610	705	815
E_{sol} [kWh]	81048	104002	99303
Q_{sol} [kWh]	60026	93666	89076
$E_{el,net}$ [kWh]	12508	19595	19222
$\bar{\eta}_{global}$	15.43%	18.84%	19.36%
f_{dumped}	25.94%	9.94%	10.30%
$f_{capacity}$	15.94%	24.97%	24.49%

Table 6: Performance of the *base-case* and *advanced* systems designed for $DNI_{DP,opt}$ and a Typical Meteorological Year (TMY).

In order to clarify the previous discussion further, Fig. 16 shows the difference in power production between the *base-case* and *advanced* systems sized for 800 W/m^2 and the optimum DNI (Table 6); these results correspond to the week 18-25 of June of the TMY in Seville. It becomes evident

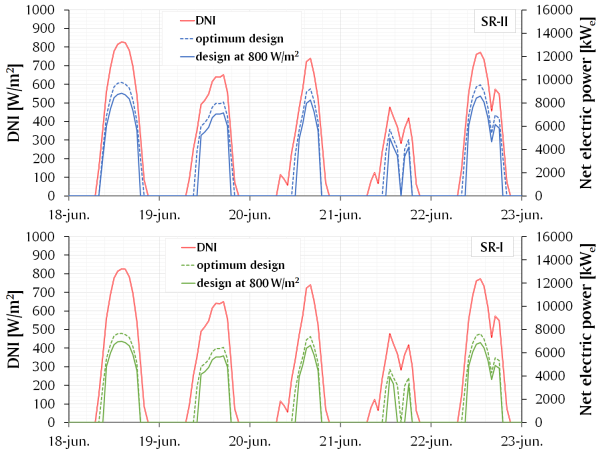

Figure 16: Power generation of the *base-case* (below) and *advanced* (above) systems sized for 800 W/m^2 (green and blue solid lines) and for the optimum DNI (green and blue dotted lines) between June 19^{th} and June 22^{nd} of the TMY.

that the dashed lines representing the optimized system are always above the solid lines representing the system designed for 800 W/m^2. This increases the capacity factor of the system and is expected to consequently reduce the levelized cost of electricity.

6. Conclusions

An innovative integrated procedure to design solar power generators based on micro gas turbines and parabolic dish collectors has been presented with a specific focus on the geometry and specifications of the components that yield the best annual performance. This methodology includes a control strategy aimed at avoiding overheating and overloading of the system under any operating conditions (DNI and ambient temperature).

The design model was run for two different sets of turbine inlet temperatures and recuperator effectiveness (TIT and $\varepsilon_{rec,DP}$): 800°C-85% for the *base-case* and 900°C-90% for the *advanced* system. Different systems are designed for each case, yielding different off-design performance maps that link the net power output of the system to the boundary conditions of the site (ambient temperature and DNI).

With this information, annual simulations were performed for three selected locations (Beijing, Seville and San Diego) based on standard perfor-

mance maps for a reference DNI and on designs tailored to their particular DNI. The results show that there is a large potential for performance gain when the system is designed with a project-specific DNI_{DP} in lieu of a standard DNI_{DP} (800 W/m^2). For the cases considered, the mean annual conversion efficiency of the *base-case* and *advanced* systems can potentially increase by 11-16% and 14-19% respectively.

Finally, with regards to the annual production of electricity, the figures in the previous paragraph translate into a very large increase which can be as high as almost 50% for the case of Beijing. These results emphasize the importance of selecting the design specifications in accordance with the local meteorological conditions along a typical year in order to maximize the production of electricity and in turn minimize costs.

7. Acknowledgments

This paper has partly been funded by the European Commission under Grant Agreement No. 308952 of the 7^{th} Framework Programme: *Optimised Microturbine SOlar Power system - OMSoP*. The authors are also grateful to the OMSoP consortium members for sharing technical information used to fine tune the model of performance presented herein.

8. References

[1] R. Buck, T. BraÌĹuning, T. Denk, M. PfaÌĹnder, P. SchwarzboÌĹzl, F. Tellez, Solar-hybrid gas turbine-based power tower systems (refos), Journal of Solar Energy Engineering 124 (1) (2002) 2–9.

[2] P. Schwarzbözl, R. Buck, C. Sugarmen, A. Ring, M. J. M. Crespo, P. Altwegg, J. Enrile, Solar gas turbine systems: design, cost and perspectives, Solar Energy 80 (10) (2006) 1231–1240.

[3] C. Sugarmen, F. Tellez, R. Buck, J. Medina, P. Altwegg, A. Ring, M. Romero, P. Heller, P. Schwarzbözl, Solgate: Solar hybrid gas turbine electric power system, Final Report.

[4] M. Quero, R. Korzynietz, M. Ebert, A. Jiménez, A. Del Río, J. Brioso, Solugas–operation experience of the first solar hybrid gas turbine system at mw scale, Energy Procedia 49 (2014) 1820–1830.

[5] R. Korzynietz, J. Brioso, A. del Río, M. Quero, M. Gallas, R. Uhlig, M. Ebert, R. Buck, D. Teraji, Solugas–comprehensive analysis of the solar hybrid brayton plant, Solar Energy 135 (2016) 578–589.

[6] ETN, Omsop project (2013).
URL `https://omsop.serverdata.net/`

[7] A. Giovannelli, State of the art on small-scale concentrated solar power plants, Energy Procedia 82 (2015) 607–614.

[8] E. OMSOP, Project, deliverable d3.4-report on state-of-the-art dish-engine applications, july 2013.

[9] M. Lanchi, M. Montecchi, T. Crescenzi, D. Mele, A. Miliozzi, V. Russo, D. Mazzei, M. Misceo, M. Falchetta, R. Mancini, Investigation into the Coupling of Micro Gas Turbines with CSP Technology: OMSoP Project, Energy Procedia 69 (2015) 1317 – 1326.

[10] G. Cerri, I. Bernardini, A. Giovannelli, L. Chennaoui, A gas turbine high efficiency cycle fed by concentrated solar power.

[11] D. SÃąnchez, A. Bortkiewicz, J. M. RodrÃŋguez, G. S. MartÃŋnez, G. Gavagnin, T. SÃąnchez, A methodology to identify potential markets for small-scale solar thermal power generators, Applied Energy 169 (2016) 287 – 300.

[12] G. Gavagnin, D. Sánchez, G. S. Martínez, J. M. Rodríguez, A. Muñoz, Cost analysis of solar thermal power generators based on parabolic dish and micro gas turbine: Manufacturing, transportation and installation, Applied Energy 194 (2017) 108–122.

[13] G. Gavagnin, D. Sánchez, J. Rodríguez, A. Muñoz, G. Martínez, Economic Competitiveness of Dish-mGT Solar Power Generators (GT2017-64351), in: ASME-IGTI (Ed.), ASME 2017 Turbo Expo: Turbine Technical Conference and Exposition, Charlotte, NC, 2017.

[14] W. Visser, S. Shakariyants, M. Oostveen, Development of a 3 kW Microturbine for CHP applications, Journal of Engineering for Gas Turbines and Power 133 (2011) 042301.

[15] T. Hynes, The most eficient small gas turbines in the world, in: Eco-summit, Berlin, 2017.

[16] C. Soares, Microturbines: applications for distributed energy systems, Butterworth-Heinemann, 2011.

[17] K. Lovegrove, W. Stein, Concentrating solar power technology: principles, developments and applications, Elsevier, 2012.

[18] L. Aichmayer, J. Spelling, W. Wang, B. Laumert, Design and analysis of a solar receiver for micro gas turbine based solar dish systems, in: International SolarPACES Conference 2012. Marrakesh, Morocco. September 11-14, 2012.

[19] L. Aichmayer, J. Spelling, B. Laumert, Preliminary design and analysis of a novel solar receiver for a micro gas-turbine based solar dish system, Solar Energy 114 (2015) 378–396.

[20] W. Wang, H. Xu, B. Laumert, T. Strand, An inverse design method for a cavity receiver used in solar dish brayton system, Solar Energy 110 (2014) 745–755.

[21] L. Aichmayer, J. Spelling, B. Laumert, T. Fransson, Micro gas-turbine design for small-scale hybrid solar power plants, Journal of engineering for gas turbines and power 135 (11) (2013) 113001.

[22] L. Aichmayer, J. Spelling, B. Laumert, Small scale hybrid solar power plants for polygeneration in rural areas, Energy Procedia 57 (2014) 1536–1545.

[23] L. Aichmayer, J. Spelling, B. Laumert, Thermoeconomic analysis of a solar dish micro gas-turbine combined-cycle power plant, Energy Procedia 69 (2015) 1089–1099.

[24] W. Wang, G. Ragnolo, L. Aichmayer, T. Strand, B. Laumert, Integrated design of a hybrid gas turbine-receiver unit for a solar dish system, Energy Procedia 69 (2015) 583–592.

[25] J. Kesseli, A. Wells, Cost competitive 30 kWe gas turbine/generator demonstration for cogeneration or solar-electric applications, in: IEEE (Ed.), 24^{th} International Energy Conversion Engineering Conference, 1989, pp. 1903 – 1908.

[26] B. Dickey, Test Results From a Concentrated Solar Microturbine Brayton Cycle Integration GT2011-45918, in: ASME-IGTI (Ed.), ASME 2011 Turbo Expo: Turbine Technical Conference and Exposition, 2011, pp. 2013–1036.

[27] W. G. Le Roux, J. P. Meyer, Modeling the small-scale dish-mounted solar thermal brayton cycle, in: SOLARPACES 2015: International Conference on Concentrating Solar Power and Chemical Energy Systems, Vol. 1734, AIP Publishing, 2016, p. 060002.

[28] S. Semprini, D. Sánchez, A. De Pascale, Performance analysis of a micro gas turbine and solar dish integrated system under different solar-only and hybrid operating conditions, Solar Energy 132 (2016) 279–293.

[29] S. Alavi, I. Bernardini, G. Cerri, L. Chennaoui, S. Mazzoni, Mgt cycles for solar dish applications, 3rd Southern African Solar Energy Conference, South Africa, 11-13 May, 2015., 2015.

[30] L. D. Jaffe, A review of test results on solar thermal power modules with dish-mounted stirling and brayton cycle engines, Journal of solar energy engineering 110 (4) (1988) 268–274.

[31] W. B. Stine, R. B. Diver, A compendium of solar dish/stirling technology, Tech. rep., DTIC Document (1994).

[32] J. Coventry, C. Andraka, Dish systems for {CSP}, Solar Energy.

[33] R. L. Johnson, Subatmospheric brayton-cycle engine program review, Tech. rep., AiResearch Mfg. Co., Torrance, CA (USA) (1984).

[34] E. staff of Garrett Turbine Engine Componay, Brayton cycle solarized advanced gas turbine: Final report, Tech. rep., NASA (1986).

[35] L. Amsbeck, T. Denk, M. Ebert, C. Gertig, P. Heller, P. Herrman, J. Jedamski, J. John, P. Tobias, J. Rehn, Test of a solar-hybrid microturbine system and evaluation of storage deployment.

[36] B. Dickey, Test results from a concentrated solar microturbine brayton cycle integration, in: ASME 2011 Turbo Expo: Turbine Technical Conference and Exposition, American Society of Mechanical Engineers, 2011, pp. 1031–1036.

[37] J. Kesseli, Brayton power conversion system, Tech. rep., Brayton Energy (2012).

[38] P. Heller, R. Buck, T. Biehler, Development of a Volumetric Receiver for a Dish-Brayton System, in: ASME (Ed.), ASME Joint Solar Engineering Conference, 1996.

[39] R. Buck, P. Heller, H. Koch, Receiver development for a Dish-Brayton system, in: ASME (Ed.), ASME International Solar Energy Conference, San Antonio, TX, 1996.

[40] C. Rodgers, C. F. McDonald, Small recuperated gas turbine APU concept to abate concern about emissions, high fuel cost, and noise, in: ASME Turbo Expo 2007: Power for Land, Sea, and Air, Montreal, Canada, 2007, pp. 383–391.

[41] C. Rodgers, Thermo-Economics of a small 50 kW Turbogenerator, in: ASME 1997 International Gas Turbine and Aeroengine Congress and Exhibition, American Society of Mechanical Engineers, Orlando, FL, 1997.

[42] C. Rodgers, Turbochargers to small gas turbines?, in: ASME 1997 International Gas Turbine and Aeroengine Congress and Exhibition, Orlando, FL, 1997.

[43] P. F. Myers, Economics and Design Approaches for Small Commercial Turbogenerators, in: ASME 1997 International Gas Turbine and Aeroengine Congress and Exhibition, Orlando, FL, 1997.

[44] C. F. McDonald, C. Rodgers, The ubiquitous personal turbine - A power vision for the 21st century, in: ASME Turbo Expo 2001: Power for Land, Sea, and Air, New Orleans, LO, 2001.

[45] D. Gallup, J. Kesseli, A solarized Brayton engine based on turbo-charger technology and the DLR receiver, in: Intersociety Energy Conversion Engineering Conference, Vol. 4, American Nuclear Society, 1994, pp. 1719–1719.

[46] A. Giostri, E. Macchi, An advanced solution to boost sun-to-electricity efficiency of parabolic dish, Solar Energy 139 (2016) 337–354.

[47] G. Xiao, T. Yang, H. Liu, D. Ni, M. L. Ferrari, M. Li, Z. Luo, K. Cen, M. Ni, Recuperators for micro gas turbines: A review, Applied Energy 197 (2017) 83–99.

[48] I. H. Bell, J. Wronski, S. Quoilin, V. Lemort, Pure and pseudo-pure fluid thermophysical property evaluation and the open-source thermophysical property library coolprop, Industrial & Engineering Chemistry Research 53 (6) (2014) 2498–2508. arXiv:http://pubs.acs.org/doi/pdf/10.1021/ie4033999, doi:10.1021/ie4033999.
URL http://pubs.acs.org/doi/abs/10.1021/ie4033999

[49] MATLAB, version 7.10.0 (R2010a), The MathWorks Inc., Natick, Massachusetts, 2010.

[50] C. F. McDonald, Recuperator considerations for future higher efficiency microturbines, Applied Thermal Engineering 23 (12) (2003) 1463–1487.

[51] M. Ghavami, J. Alzaili, I. Sayma, A., A comparative study of the control strategies for pure concentrated solar power micro gas turbines (GT2017-63987), in: ASME-IGTI (Ed.), ASME 2017 Turbo Expo: Turbine Technical Conference and Exposition, 2017.

[52] R. H. Aungier, Centrifugal compressors (2000).

[53] R. H. Aungier, Turbine aerodynamics, American Society of Mechanical Engineers Press, New York.

[54] B. Monge, Design of supercritical carbon dioxide centrifugal compressors, University of Seville.

[55] S. M. Futral Jr, D. E. Holeski, Experimental results of varying the blade-shroud clearance in a 6.02-inch radial-inflow turbine.

[56] C. National Renewable Energy Laboratory. Golden, System advisor model version 2016.3.14 (sam 2016.3.14)., https://sam.nrel.gov/content/downloads. (October 2016).

[57] M. J. Moran, H. N. Shapiro, D. D. Boettner, M. B. Bailey, Fundamentals of engineering thermodynamics, John Wiley & Sons, 2010.

[58] B. M. Gallo, M. S. El-Genk, J.-M. Tournier, M. S. El-Genk, Compressor and turbine models of brayton units for space nuclear power systems, in: AIP Conference Proceedings, Vol. 880, AIP, 2007, pp. 472–482.

[59] C. Rodgers, Microturbine rotational speed selection, in: ASME Turbo Expo 2013: Turbine Technical Conference and Exposition, American Society of Mechanical Engineers, 2013, pp. V05AT23A005–V05AT23A005.

[60] O. Balje, A study on design criteria and matching of turbomachines: Part aâĂŤsimilarity relations and design criteria of turbines, Journal of Engineering for Power 84 (1) (1962) 83–102.

[61] O. Balje, A study on design criteria and matching of turbomachines: Part bâĂŤcompressor and pump performance and matching of turbocomponents, Journal of Engineering for Power 84 (1) (1962) 103–114.

[62] O. Balje, A study on reynolds number effects in turbomachines, Journal of Engineering for Power 86 (3) (1964) 227–235.

[63] A. J. Head, W. Visser, Scaling 3-36kw microturbines, in: ASME Turbo Expo 2012: Turbine Technical Conference and Exposition, American Society of Mechanical Engineers, 2012, pp. 609–617.

[64] C. Rodgers, A cycle analysis technique for small gas turbines, Solar Division (1969) 37–49.

[65] J. Nikuradse, Laws of flow in rough pipes, National Advisory Committee for Aeronautics Washington, 1950.

[66] J. E. Hesselgreaves, R. Law, D. Reay, Compact heat exchangers: selection, design and operation, Butterworth-Heinemann, 2016.

[67] R. Shah, Compact heat exchangers for microturbines.

[68] C. F. McDonald, Low-cost compact primary surface recuperator concept for microturbines, Applied Thermal Engineering 20 (5) (2000) 471–497.

[69] A. Traverso, A. F. Massardo, Optimal design of compact recuperators for microturbine application, Applied Thermal Engineering 25 (14) (2005) 2054–2071.

[70] M. Röger, C. Rickers, R. Uhlig, F. Neumann, C. Polenzky, Infrared-reflective coating on fused silica for a solar high-temperature receiver, Journal of Solar Energy Engineering 131 (2) (2009) 021004.

[71] J. R. Welty, C. E. Wicks, G. Rorrer, R. E. Wilson, Fundamentals of momentum, heat, and mass transfer, John Wiley & Sons, 2009.

[72] W. B. Stine, R. W. Harrigan, Solar energy fundamentals and design, John Wiley and Sons, Inc., New York, NY, 1985.

[73] W. B. Stine, M. Geyer, Power from the Sun, Power from the sun. net, 2001.

[74] J. A. Harris, W. S. Duff, Focal plane flux distributions produced by solar concentrating reflectors, Solar Energy 27 (5) (1981) 403–411.

[75] J. Noall, M. Forsha, Off-design turbomachinery performance mapping, Barber Nichols Inc., Internal Program Report.

[76] A. J. Glassman, Turbine design and application. nasa sp-290, NASA Special Publication 290.

Appendix A. Design models

This Section presents the equations and solving procedures implemented in each design module of the flowchart in Fig. 3.

Appendix A.1. Thermodynamic cycle

The modules calculating the design thermodynamic cycle in Fig. 3 ("*Thermodynamic cycle 1 and 2*") are based on the application of mass and energy conservation and component efficiencies [57]. Thus, the outlet conditions from compressor and expander are calculated from the total-to-total pressure ratios and the isentropic efficiencies whilst the inlet and outlet states of the recuperator are computed from a fixed effectiveness and pressure loss factor ($\varepsilon_{reg,DP}$, $f_{p,cold,DP}$ and $f_{p,hot,DP}$ in Table 1). With this information, the model calculates all the thermodynamic states in Fig. 1 along with the shaft output for a given mass flow rate at compressor inlet ($\dot{m}_1$=0.1 kg/s). The net electric output is then calculated by merely applying electric and mechanical efficiencies.

Appendix A.2. Turbomachinery

The design modules of compressor and turbine provide the total-to-total isentropic efficiencies and the rotational speed of the sized stages [58], based on the one-dimensional approaches proposed by Aungier in [52] and [53]. In the main, this approach assumes constant flow field variables (velocity, temperature and pressure) at each cross-section of the flow passage (channel). These variables are obtained from steady-state mass, energy and momentum balance equations computed along the mean stream surface using empirical fluid dynamics and total pressure loss correlations. A boundary layer model is applied to take into account the total pressure loss due to skin friction between the fluid and passage walls, with the resulting variation of Reynolds number along the mean stream surface being used to evaluate the entropy rise and, in turn, the isentropic efficiency.

The matching of compressor and turbine is initiated in the turbine assuming a reference specific speed $n_{s,t}$=0.55 on the based on recommendations by Rodgers [59] and Aungier [53], Eq. (A.1). Based on this value, it is possible to calculate the rotational speed that yields highest turbine efficiency [60, 61]. This is then used along with the spouting velocity $c_{0,is}$ (velocity obtained in a total-to-static isentropic expansion) to calculate the tangential speed of the blade ($u_{tip,t}$) and the corresponding rotor diameter ($d_{tip,t}$), Eq. (A.2) as described by Aungier [53].

$$\omega_{DP} = n_{s,t} \frac{\Delta h_{s,t}^{0.75}}{\sqrt{\dot{v}_{out}}} \tag{A.1}$$

$$\nu_{ts,t} = \frac{u_{tip}}{c_{0,is}} = 0.737 \cdot n_{s,t}^{0.2} \tag{A.2}$$

The rotational speed of the compressor is the same as that of the expander and it can be used to calculate the specific speed ($n_{s,c}$) and diameter ($d_{s,c}$) of this machine, Eqs. (A.3,A.4). This information is obtained by interpolating the corresponding n_s vs. d_s chart for maximum compressor efficiency (*Cordier* line, shown dashed red in Fig. A.1) in the range of application of radial turbomachinery: $50<n_{s,c}<100$ [62]. The specific diameter ($d_{s,c}$) so obtained is used to calculate the tip diameter of the impeller ($d_{tip,c}$).

$$n_{s,c} = \omega_{DP} \frac{\sqrt{\dot{v}_{in}}}{\Delta h_{s,c}^{0.75}} \tag{A.3}$$

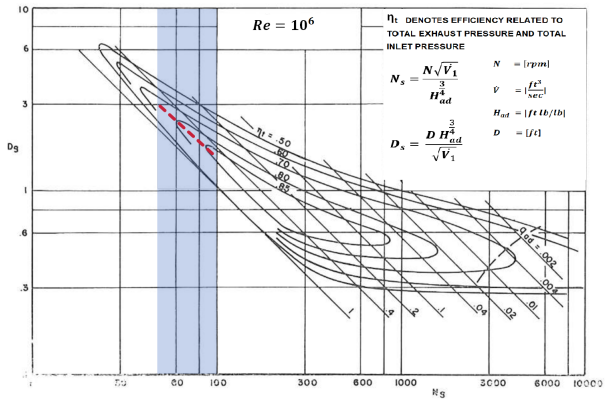

Figure A.1: Specific speed vs. specific diameter diagram of a compressor showing the *Cordier* line for radial stages in dashed red. Adapted from [62].

$$d_{s,c} = 2.865 \cdot n_{s,c}^{-0.946} = d_{tip} \frac{\Delta h_{s,c}^{0.25}}{\sqrt{\dot{v}_{in}}} \tag{A.4}$$

The sizing of the turbine is performed in the following order: rotor, nozzle, inlet volute and exhaust diffuser. For these elements, a draft geometry is produced from a set of default design specifications in combination with empirical correlations based on the reference specific speed, as suggested by Aungier [53]. These specifications include the spouting velocity of the stage, specific diameter of the rotor, inlet flow angle, number, chord and thickness of the blades and inlet-to-outlet radii ratio of the nozzle. The main design steps applied to these data are summarized below, as described in [53] where more details can be found:

- The main geometrical parameters of the rotor are calculated from $n_{s,t}$ and $d_{tip,t}$ under the assumption that inlet velocity is radial (relative rotor inlet angle is 90°):
  - The meridional plane of the turbine is sized so as to minimize the variation of area between the inlet and outlet sections under the constant mass flow rate restriction, Fig. A.2.
  - The number, mean line geometry and thickness distribution of the blades is calculated with empirical correlations.
  - The feasibility of the resulting geometry is verified against the specific guidelines proposed by Aungier [53].

- In order to size the nozzle, the minimum number of blades needed to yield radial relative flow at the inlet to the wheel and, at the same time, a blade loading lower than 1 is calculated.

- An elliptical configuration is considered for the volute, where the variation of cross sectional area comes determined by mass conservation, a constant size parameter SP=1 and angular momentum conservation at nozzle inlet.

$$SP = \frac{\sqrt{\dot{v}_{out}}}{\Delta h_s^{0.25}} = 1 \tag{A.5}$$

- The design of the exhaust diffuser is obtained from empirical correlations on the assumptions that the ratio between outlet and inlet areas is equal to 1.5 and that the divergence angle is 11°.

The aforedescribed procedure generates a draft geometry for the actual design point, yielding a certain mass flow rate and total-to-total expansion ratio. These values are then used to correct the design until the target values are attained. Once the final design is obtained, the corresponding performance map is produced by merely calculating the performance of the expander for different sets of boundary conditions, including the specific conditions for which sections of the machine get choked.

The compressor design process does not start from a set of specifications but it is carried out directly by means of the empirical performance model proposed by Aungier [52]. In this, guessed values of the total-to-total isentropic efficiency and total pressure loss coefficient (from rotor inlet to volute outlet) are initially assumed and the geometry of each component of the compressor is evaluated as follows:

- The impeller inlet section is sized in order to minimize the relative Mach number at the shroud, whilst the outlet diameter is influenced by the blade exit angle as a result of a trade-off between stage work and distortion, and slip factors for each $d_{tip,c}$; this is shown in Eqs. (A.3,A.4) and in Fig. A.2. The number of blades results from the minimum value yielding a blade loading lower than 0.9.

- The diffuser can be of the vaned or vaneless type. In the former case, the number of vanes, the area ratio and the divergence angle result from an optimization process to yield maximum efficiency with a total load lower than 0.3.

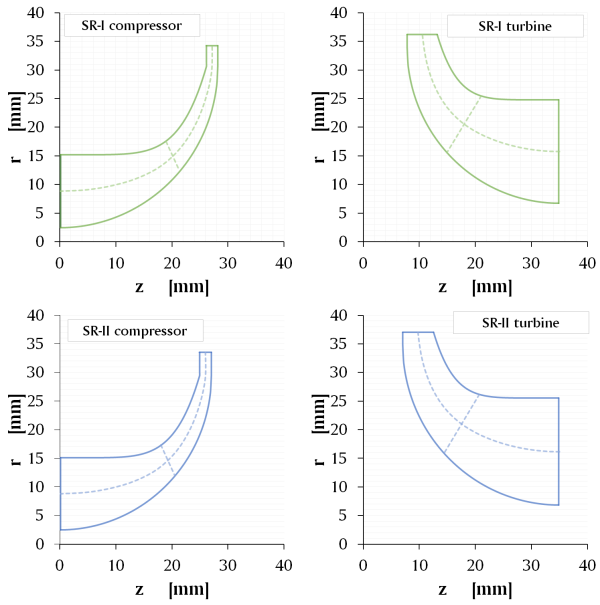

Figure A.2: Meridional flow passage of the compressor impeller (left) and turbine wheel (right) for the *base-case* (above) and *advanced* (below) systems.

- The outlet radius of the volute is calculated iteratively by fixing a size parameter of 1.05. The radius distribution is then obtained from continuity by keeping the size parameter constant.

To properly take into account the strong influence of the clearance gap between rotor and shroud (casing) [63, 64] the following definition is used:

$$\delta_{cl} = \delta_{cl,ref} \cdot \left(\frac{b_{blade}}{b_{blade,ref}} \right)^{0.6}, \tag{A.6}$$

where the reference blade height is $b_{blade,ref} = 5$ mm and the reference gap $\delta_{cl,ref}$ is 0.4 mm and 0.3 mm for turbines and compressors, respectively. Finally, the effect of roughness is accounted for with a simple skin friction model based on boundary layer analysis in which a peak-to-valley roughness of 1 µm is assumed [65].

The performance maps of compressor and turbine for the *base-case* and *advanced* systems are shown in Fig. A.4. These maps show total-to-total isentropic enthalpy change and isentropic efficiency versus mass flow rate for shaft speeds ranging from 70% to 115% of the design point value.

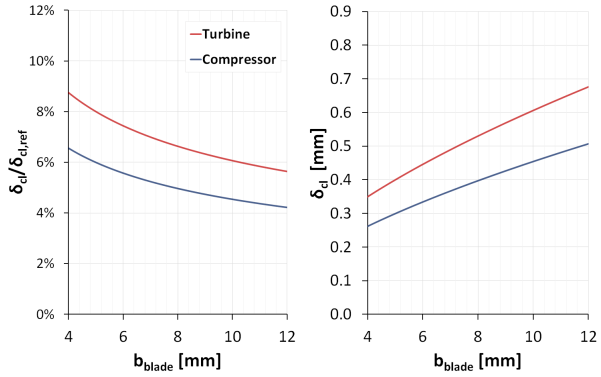

Figure A.3: Relative (left) and absolute clearance (right) gaps vs. blade height distributions.

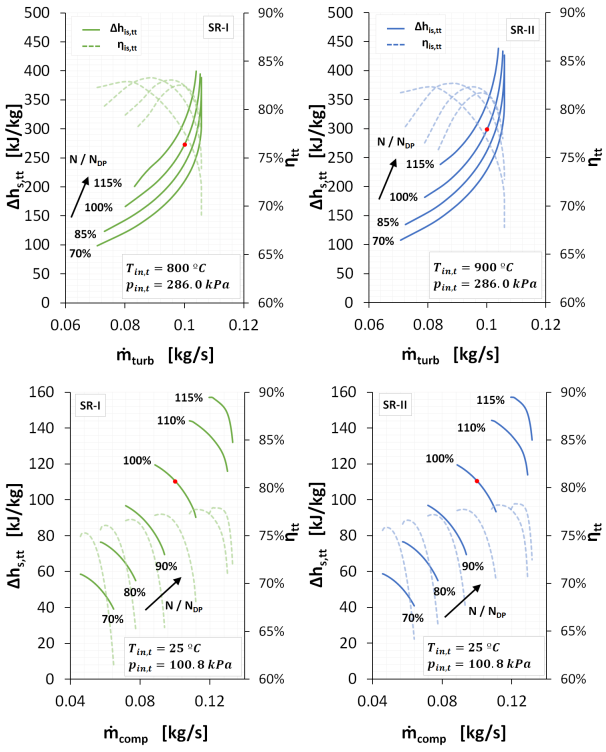

Figure A.4: Turbine (above) and compressor (below) maps for the *base-case* (left) and *advanced* (right) systems: total-to-total isentropic enthalpy change vs. mass flow rate (solid) and total-to-total isentropic efficiency vs. mass flow rate (dashed).

Appendix A.3. Recuperator

The design model of the regenerator is based on the well-know $\varepsilon - NTU$ approach [66], based on the inlet and outlet design conditions calculated with the "*Thermodynamic cycle 1 and 2*" modules in Fig. 3. The rated global heat transfer coefficient is initially set to a constant value of $U_{r,DP} = 100$ W/m^2·K and then the hot and cold heat capacities ($\dot{C}_{DP} = \dot{m}_{DP} \cdot \bar{c}_{p,DP}$) and heat capacity ratio ($C^*_{DP} = \dot{C}_{min,DP}/\dot{C}_{max,DP}$) are calculated, yielding the number of transfer units NTU_{DP} and the total heat transfer area $A_{ex,r}$ at the design point:

$$NTU_{DP} = \frac{\log_e \frac{1-\varepsilon_{rec,DP}}{1-C^*_{DP}\cdot\varepsilon_{rec,DP}}}{\dot{m}_{in,DP} \cdot \Delta h_{rec,DP}} \tag{A.7}$$

$$HTA_{rec} = \frac{\dot{m}_{in,DP} \cdot c_{p,in,DP} \cdot NTU_{DP}}{U_{rec,DP}} \tag{A.8}$$

More considerations about the application of this method to recuperators in micro gas turbines can be found in [50, 67–69].

Appendix A.4. Cavity volumetric receiver

The simple model of the cavity volumetric receiver proposed by Aichmayer in [21] and modified by Semprini [28] to introduce the equations for grey bodies is used here, with optical properties evaluated at each specific wavelength. The model considers convective losses whereas the conductive loss and the utilization of a secondary concentrator are neglected.

The optical properties are taken from Roger [70]. They are wavelength-weighted values for a 5 mm thick fused silica glass window considering the solar radiation spectrum and the thermal radiation produced by a black body at 1100 °C. The radiation emitted by the glass window is calculated as that of a grey body at 600K (326.85°C) with emissivity and absorptivity equal to 0.8. The model includes energy conservation equations applied to the glass window, cavity and foam absorber as shown in Eqs.(A.9-A.13), with an additional equation for the absorber temperature, Eq.(A.14). In these equations, subscripts *vis* and *ir* stand for the radiative properties of the glass window of the receiver for incident light in the visible spectrum and for the incident thermal radiation generated by a blackbody at the temperature of the absorber. Then, subscript *th* indicates that the corresonding property is evaluated at the temperature of the absorber foam:

- Heat absorbed by radiation by the window ($Q_{rad,w}$):

$$\dot{Q}_{rad,w} = I \cdot \alpha_{w,vis} + \sigma \left(\alpha_{w,th} T_{amb}^4 + \alpha_{w,ir} T_s^4 - 2\epsilon_{w,th} T_w^4 \right) \tag{A.9}$$

- Window heat loss due to convection. This is made up by the external ($k_{cv,ext} \left(T_w - T_{amb} \right)$) and internal ($k_{cv,int} \left(T_w - \bar{T}_{air} \right)$) losses:

$$\dot{Q}_{cv,w} = k_{cv,ext} \left(T_w - T_{amb} \right) + k_{cv,in} \left(T_w - \bar{T}_{air} \right) \tag{A.10}$$

$$\bar{T}_{air} = \frac{T_{air,in} + T_{air,out}}{2} \tag{A.11}$$

- Energy conservation implies that $\dot{Q}_{rad,w} = \dot{Q}_{cv,w}$.

- A similar energy balance can be applied to the absorber material to calculate the net radiative heat flux absorbed:

$$\dot{Q}_{rad,abs} = I \cdot \tau_{vis} + \sigma \left(\epsilon_{w,th} T_w^4 - T_s^4 + \varsigma_{w,ir} T_s^4 \right) \tag{A.12}$$

- Finally, the amount of heat that the stream of air exchanges with the absorber material and window is expressed as follows:

$$G \Delta h_{air} = k_{cv,int} (T_w - \bar{T}_{air}) + k_{cv,abs} (T_{abs} - T_4) \tag{A.13}$$

- An estimate of the absorber temperature is provided by the following equation:

$$T_{abs} = \frac{\bar{T}_{air} + T_{air,out}}{2} \tag{A.14}$$

The convective heat transfer coefficient on the outer wall of the window is based on a Nusselt number correlation for natural convection flow on inclined planes $h_{conv,DP} = f(\xi_{incl})$ where the inclination angle is set to a constant value $\xi_{incl} = 60°$ [71]. With all this information, the outcome of the energy balance is expressed in terms of specific intercepted beam power ($I_{DP} = \dot{Q}_{int,DP} / A_{rcv}$) and specific air mass flow rate per unit window area ($G_{DP} = \dot{m}_{3,DP} / A_{rcv}$).

Appendix A.5. Parabolic dish collector

This Section describes the fundamentals of the collector model, the complete description of which can be found in [72, 73]. The concentrator geometry is a truncated portion of a paraboloid, the extent of which is defined by the rim angle ψ_{rim}. This parameter, whose value is set to $\psi_{rim} = 45°$ in this work in order to maximize the concentration ratio between the parabolic dish and the cavity receiver, can actually be correlated to the ratio between aperture diameter d_{dish} and focal length f_{dish} as shown in Eq. (A.15).

$$f_{dish} = \frac{d_{dish}}{4 \tan\left(\frac{\psi_{rim}}{2}\right)} \tag{A.15}$$

The amount of energy collected and concentrated by the collector on the receiver window is calculated under the assumption of a perfect parabola, and then evaluating the deviations from such ideal collector due to reflection of non-parallel rays (sun shape error) and other errors. These are assumed to be random and are reported in the form of standard deviation units so that it is possible to determine their combined effect statistically. The total concentration error ($e_{tot} = 6.7$ mrad) is considered constant and calculated as the cumulative effect of the Sun shape effect, the slope error of the true parabolic shape, the non-specular reflection of the incident beam, the tracking error and the receiver alignment error. Table A.1 shows the breakdown of the angular concentration errors considered for one standard distribution; i.e., when 68% of all measurements of the errors fall within the angular deviations noted. As a final effect, the radiation emitted by the Sun is not evenly distributed across its disc and hence a standard distribution is assumed to handle this error as an additional contribution to the aforedescribed non-ideal behavior, according to Harris and Duff [74].

Concentration errors		
Type and source	Effective magnitude ($1e$)	e^2
Structure	5 mrad	25
Tracking sensor	2 mrad	4
Tracking drive non-uniformity	2 mrad	4
Receiver alignment	2 mrad	4
Total 1D	6.1 mrad	37
Mirror specular reflectance	0.5 mrad	0.25
Sun shape	2.8 mrad	7.84
Total 2D	2.8 mrad	8.09
Total	6.7 mrad	

Table A.1: Sun image size, reflection, tracking and alignment errors.

With all this information, and in order to calculate the total irradiance (incoming concentrated radiation onto the receiver window), the dish is divided into finite rings, each one collecting the solar energy calculated calculated by Eq.(A.16-A.19) where ς_{dish} is the specular reflectance of the mirror surface and Γ_i is the fraction of captured heat flux calculated as a function of the receiver window size, Eq.(A.18).

$$\dot{Q}_{inter,DP} = \sum_{i=3^{\circ}}^{\psi_{rim}} \varsigma_{dish} \cdot \Gamma_i \cdot \left(\frac{d\phi}{d\psi}\right)_{i,DP} \cdot \Delta\psi_i \tag{A.16}$$

$$\left(\frac{d\phi}{d\psi}\right)_{i,DP} = \frac{8\pi \cdot DNI_{DP} \cdot f_{dish}^2 \cdot \sin\psi_i}{(1+\cos\psi_i)^2} \tag{A.17}$$

$$n_i = \frac{2}{e_{tot}} \cdot \arctan\frac{d_{rec} \cdot \cos\phi_i}{2p_{dish}}; \quad \Gamma_i = f(n_i) \tag{A.18}$$

$$p_{dish} = \frac{2f_{dish}}{1+\cos(\psi_{rim})} \tag{A.19}$$

Appendix B. Off-design model

This Section presents the submodels of the solar-mGT components which are used to calculate the power output and efficiency of the total system for given DNI and ambient temperature, Fig. 4.

Appendix B.1. Turbomachinery

The off-design submodels of compressor and turbine calculate the isentropic and actual (polytropic) outlet states of these components, starting from the rotational speed and mass flow rate obtained from the characteristic performance maps (see Section Appendix A.2). These maps are corrected to extend their validity to inlet temperatures and pressures different from the rated values that were used to calculate them. Similarity laws are also used to calculate the corrected inlet conditions as suggested in [75] and [76]. Compared to the typical formulas used to correct turbomachinery maps, which are valid for perfect gas, some factors accounting for real gas effects (variable specific heats and compressibility factor) are introduced. These similarity laws correlate the inlet mass flow rate and rotational speed to the isentropic enthalpy change and isentropic efficiency as in Eqs. (B.1-B.3) where δ is the ratio between the actual and reference inlet pressures ($\delta = p_{0,act}/p_{0,ref}$) and ϵ

and θ take into account the changes in compressibility and specific heat ratio between the reference (ref) and actual ($real$) inlet conditions, Eq. (B.4,B.5).

$$N_{eq} = \frac{N_{real}}{\sqrt{\theta}} \tag{B.1}$$

$$\dot{m}_{eq} = \frac{\dot{m}_{real} \cdot \sqrt{\theta}}{\delta} \cdot \epsilon \tag{B.2}$$

$$\Delta h_{is,eq} = \frac{\Delta h_{is,real}}{\sqrt{\theta}} \tag{B.3}$$

$$\epsilon = \frac{\gamma_{ref} \cdot \left(\frac{2}{\gamma_{ref}+1}\right)^{\frac{\gamma_{ref}}{\gamma_{ref}-1}}}{\gamma_{real} \cdot \left(\frac{2}{\gamma_{real}+1}\right)^{\frac{\gamma_{real}}{\gamma_{real}-1}}} \tag{B.4}$$

$$\theta = \left(\frac{V_{cr,real}}{V_{cr,ref}}\right)^2, \tag{B.5}$$

$V_{cr,real}$ and $V_{cr,ref}$ are calculated as in Eq. (B.6) where g_c is the gravitational acceleration, Z is the gas compressibility factor and R is the ideal gas constant:

$$V_{cr} = \sqrt{\frac{2 \cdot \gamma}{\gamma + 1} \cdot g_c \cdot Z \cdot R \cdot T_{in}}. \tag{B.6}$$

Appendix B.2. Electric generator

The off-design behavior of the electric generator is simulated using the empirical model developed by ENEA for the OMSoP project [8]. In this model, the mechanical-to-electric efficiency (η_{el}) depends on rotational speed (N) and shaft work (P_{mech}), the latter of which is limited to prevent a too high current intensity in the rotor. Figure B.1 shows the non dimensional relationships of the model.

Appendix B.3. Other components

The performance of the parabolic dish collector in off-design conditions does not differ from the design point due to the two degrees of freedom of the tracking system, which ensure that the dish is aligned with the Sun at any time. The off-design models of recuperator and solar receiver include the same equations as the design models but they are solved downstream rather

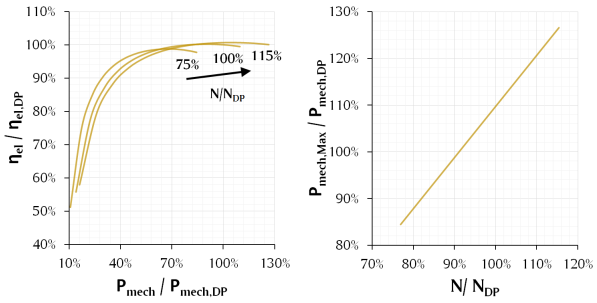

Figure B.1: Electric efficiency of generator vs. shaft work and rotational speed (left) and maximum shaft power vs. rotational speed (right). Scales are non-dimensional.

than upstream. The variations of the global heat transfer coefficient with the mass flow rate are evaluated using Eq. (B.7).

$$U = U_{DP} \cdot \left(\frac{\dot{m}}{\dot{m}_{DP}} \right)^{0.8} \tag{B.7}$$

The pressure losses of recuperator, solar receiver and inlet/outlet ducts are varied according to Eq. (B.8).

$$\Delta p = \Delta p_{DP} \cdot \left(\frac{\dot{m}}{\dot{m}_{DP}} \right)^{1.21} \cdot \frac{\rho_{DP}}{\rho} \tag{B.8}$$